Phase-field modeling of the coupled microstructure and fracture evolution in ferroelectric single crystals

Amir Abdollahi, Irene Arias

LaCàN, Universitat Politècnica de Catalunya (UPC), Campus Nord UPC-C2, E-08034 Barcelona, Spain

Abstract

We propose a phase-field model for the coupled simulation of the microstructure formation and evolution, and the nucleation and propagation of cracks in single crystal ferroelectric materials. The model naturally couples two existing energetic phase-field approaches for brittle fracture and ferroelectric domain formation and evolution. The finite element implementation of the theory in two dimensions (plane polarization and plane strain) is described. We perform, to the best of our knowledge, the first crack propagation calculations of ferroelectric single crystals, allowing simultaneously for general microstructures to develop. Previously, the microstructure calculations were performed at fixed crack configuration or under the assumption of small scale switching. Our simulations show that this assumption breaks down as soon as the crack tip field interacts with the boundaries of the test sample (or, in general, obstacles such as defects or grain boundaries). Then, the microstructure induced by the presence of the crack propagates beyond its vicinity leading to the formation of twins. The interactions between the twins and the crack are investigated under mechanical and electromechanical loadings, both for permeable and impermeable cracks, with an emphasis on the fracture toughening due to domain switching, and compared with experiments.

Keywords: Ferroelectricity, Fracture, Phase-field models, Finite element analysis, Twinning

1. Introduction

Ferroelectric ceramics are prominent materials for micro-sensors, actuators and transducers because of their unique electro-mechanical coupling properties. However, most ferroelectrics exhibit a fracture toughness similar to that of glass, on the order of 1 MPa$\sqrt{m}$. Their inherent brittleness makes them susceptible to fracture. Since practical applications often involve strong mechanical and electrical loading conditions, it is important to understand the fracture behavior of ferroelectric components, and this has been the subject of numerous investigations (see [1, 2, 3] for excellent theoretical and experimental reviews). Fracture processes in these materials are notoriously complex, mostly due to the interactions between the crack tip stress fields and the localized switching phenomena in this zone (formation and evolution of ferroelectric twins or domains) [4, 5, 6, 7]. For instance, domain

switching has been reported near various defects including cracks [8], and these switching phenomena have been made responsible for changes in the fracture behavior of ferroelectric materials. This suggests that these microscopic phenomena should be taken into account in the analysis of the global reliability of ferroelectric components.

A number of theoretical approaches have been developed to understand fracture phenomena in ferroelectric ceramics, for which linear electro-mechanical models useful for piezoelectricity bring limited insight. These include models inspired in plasticity theory and aimed at polycrystalline ferroelectric ceramics [9]. These models do not intend to describe explicitly the domain formation, but rather the effective phenomenology [7, 10]. Other models rely on a simple local switching criterion [11], which under the assumption of small-scale switching, have allowed researchers to analyze the local phase transformations near the crack tip [12, 13, 14]. In the last years, another family of continuum models that aim at explicitly describing the formation and evolution of individual ferroelectric domains in single crystals has gained impetus, namely Devonshire-Ginzburg-Landau (TDGL) phase-field models of ferroelectric materials or related models [15, 16, 17, 18, 19]. See [20] and [21] for related models in micromagnetics. These microstructural models have specifically been applied to fracture, in all cases with a fixed crack. The formation of domains near a crack tip has been studied under applied electromechanical loadings, and the influence on the mechanical $J-$integral has been reported [22]. The small-scale switching patterns of simplified models have been investigated with phase-field models [23]. For completeness, we mention that cohesive theories aimed at fracture in ferroelectric materials have been proposed [24, 25].

Here, the objective is to analyze the quasi-static crack propagation and the ferroelectric domain formation and evolution under combined electro-mechanical loads by tackling the full complexity of the phenomenon, with the goal of linking the microstructural details with the macroscopic observable response. For this purpose, we propose a coupled phase-field model for both the brittle crack propagation and the microstructure evolution. In complex moving interface problems such as fracture in ferroelectric ceramics, phase-field models are particularly interesting since a single partial differential equation governing the phase-field accomplishes at once (1) the tracking of the interfaces in a smeared way (cracks, domain walls) and (2) the modeling of the interfacial phenomena such as domain-wall energies or crack face boundary conditions. Furthermore, the variational nature of these models makes the coupling of multiple physics very natural. Such a model has no difficulty in describing the nucleation of domains and cracks, and tracking the evolution of the domain boundaries and crack tips. This flexibility comes at the expense of a high computational cost, since the width of the phase-field regularizations of the domain wall and the crack must be resolved by the discretization. Furthermore, the specific interface boundary or jump conditions under consideration must be encoded into the phase-field framework.

To analyze quasi-static brittle fracture, we consider a variational regularized model of Griffith's fracture that admits a straightforward numerical implementation [26, 27, 28, 29, 30]. This model and its numerical discretization allows naturally for crack nucleation, branching, and interaction between multiple cracks. It smears the crack in contrast with cohesive methods [31, 32] and other sharp crack models such as the extended finite element method

(XFEM) [33], or the strong discontinuity approach [34]. For the ferroelectric response, we follow the Devonshire-Ginzburg-Landau phase-field model presented in [15].

The theory of the proposed coupled phase-field model is introduced in Section 2. The simulation results for a simple yet informative setup of a rectangular sample under mechanical and electro-mechanical loadings are reported in Section 3. In order to elucidate the effect of each type of load, only mechanical loading is considered at first. The results for combined electro-mechanical loading are presented next and compared to the previous ones. Both electrically permeable and impermeable crack conditions are considered. Section 4 summarizes the main results of the paper.

2. Phase-field model for brittle fracture in ferroelectric materials

The two phase-field variational models for ferroelectric materials [15] and brittle fracture [27] are described separately. Then, their natural coupling and its numerical implementation is described in the case of plane polarization and plane strain.

2.1. Phase-field model for ferroelectric single crystals

The Helmholtz free energy density of a ferroelectric material is stated as [15, 18]

$$\psi(\boldsymbol{\varepsilon}, \mathbf{p}, \nabla\mathbf{p}, \mathbf{D}) = U(\nabla\mathbf{p}) + W(\mathbf{p}, \boldsymbol{\varepsilon}) + \chi(\mathbf{p}) + \frac{1}{2\varepsilon_0}(\mathbf{D} - \mathbf{p}) \cdot (\mathbf{D} - \mathbf{p}), \tag{1}$$

where $\boldsymbol{\varepsilon}$ is the strain tensor associated with the mechanical displacement $\boldsymbol{u}$, $\boldsymbol{\varepsilon} = 1/2(\nabla\boldsymbol{u} + \nabla^T\boldsymbol{u})$, $\mathbf{p}$ is the polarization, U is the domain wall energy density penalizing sharp variations in the polarization, χ is the phase separation potential, and W is the electroelastic energy density. These two last energy densities penalize deviations from the spontaneous polarizations and strains of the material, hence introducing the anisotropy and nonlinearity of ferroelectric materials. The first three terms in (1) indicate the free energy of the material. The last term is the free energy of the free space occupied by the material or the depolarization energy density [35]. It involves the polarization and the electric displacement $\mathbf{D} = \mathbf{p} - \varepsilon_0\nabla\phi$, where ϕ is the electric potential and ε_0 is the permittivity of free space. Following a Legendre transformation, the electro-mechanical enthalpy density h is obtained [18]

$$\begin{aligned} h(\boldsymbol{\varepsilon}, \mathbf{p}, \nabla\mathbf{p}, \mathbf{E}) &= \min_{\mathbf{D}} \left[\psi(\boldsymbol{\varepsilon}, \mathbf{p}, \nabla\mathbf{p}, \mathbf{D}) - \mathbf{E} \cdot \mathbf{D}\right] \\ &= U(\nabla\mathbf{p}) + W(\mathbf{p}, \boldsymbol{\varepsilon}) + \chi(\mathbf{p}) - \frac{\varepsilon_0}{2}|\mathbf{E}|^2 - \mathbf{E} \cdot \mathbf{p}, \end{aligned} \tag{2}$$

where $\mathbf{E}$ is the electric field defined as $\mathbf{E} = -\nabla\phi$. The stresses and electric displacements are derived from the electrical enthalpy as $\boldsymbol{\sigma} = \partial h/\partial\boldsymbol{\varepsilon}$ and $\mathbf{D} = -\partial h/\partial\mathbf{E}$. The energy functions U, W and χ in (1) are chosen following [36, 37], adapted to a plane polarization and plane strain state:

$$U(p_{i,j}) = \frac{a_0}{2}(p_{1,1}^2 + p_{1,2}^2 + p_{2,1}^2 + p_{2,2}^2), \tag{3}$$

$$W(p_i, \varepsilon_{jk}) = -\frac{b_1}{2}(\varepsilon_{11}p_1^2 + \varepsilon_{22}p_2^2) - \frac{b_2}{2}(\varepsilon_{11}p_2^2 + \varepsilon_{22}p_1^2) - b_3(\varepsilon_{21} + \varepsilon_{12})p_1p_2 + \frac{c_1}{2}(\varepsilon_{11}^2 + \varepsilon_{22}^2) + c_2\varepsilon_{11}\varepsilon_{22} + \frac{c_3}{2}(\varepsilon_{12}^2 + \varepsilon_{21}^2), \quad (4)$$

$$\chi(p_i) = \alpha_1(p_1^2 + p_2^2) + \alpha_{11}(p_1^4 + p_2^4) + \alpha_{12}(p_1^2p_2^2) + \alpha_{111}(p_1^6 + p_2^6) + \alpha_{112}(p_1^2p_2^4 + p_2^2p_1^4) + \alpha_{1111}(p_1^8 + p_2^8) + \alpha_{1112}(p_1^6p_2^2 + p_2^6p_1^2) + \alpha_{1122}(p_1^4p_2^4), \quad (5)$$

where the combination of energy functions χ and W is the total Landau-Devonshire energy density, a_0 is the scaling parameter of the domain wall energy, $b_i(i = 1, 2, 3)$ are the constants of the coupling terms between strain and polarization and $c_i(i = 1, 2, 3)$ are the elastic constants. The coupling constants $b_i(i = 1, 2, 3)$ are obtained by fitting the spontaneous strains of the tetragonal phase relative to the cubic phase. The phase separation energy χ is improved by adding the eighth-order terms with coefficients α_{1111}, α_{1112} and α_{1122} to reproduce the dielectric behavior of barium titanate ($BaTiO_3$) single crystals [38, 39]. The eighth-order term with coefficient α_{1122} enables the model to fit the dielectric constants while retaining a reasonable energy barrier for 90^0 domain switching in the tetragonal phase [15]. α_1 is linearly dependent on temperature and its negative value makes the cubic phase unstable. α_{111} is estimated by fitting the spontaneous polarization of the tetragonal phase. α_{112} and α_{1112} are fitted to the dielectric permitivity perpendicular to the spontaneous polarization. α_{11}, α_{12} and α_{1111} are evaluated from linear and nonlinear dielectric measurements above the Curie temperature [39]. For convenience, dimensionless variables are selected through the following normalizations: $x_i' = x_i\sqrt{c_0/a_0}/p_0$, $p_i' = p_i/p_0$, $t' = tc_0/\mu p_0^2$, $\varepsilon_0' = \varepsilon_0 c_0/p_0^2$, $\phi' = \phi/\sqrt{a_0c_0}$, $\alpha_1' = \alpha_1 p_0^2/c_0$, $\alpha_{11}' = \alpha_{11}p_0^4/c_0$, $\alpha_{12}' = \alpha_{12}p_0^4/c_0$, $\alpha_{111}' = \alpha_{111}p_0^6/c_0$, $\alpha_{112}' = \alpha_{112}p_0^6/c_0$, $\alpha_{1111}' = \alpha_{1111}p_0^8/c_0$, $\alpha_{1112}' = \alpha_{1112}p_0^8/c_0$, $\alpha_{1122}' = \alpha_{1122}p_0^8/c_0$, $b_i' = b_i p_0^2/c_0$ and $c_i' = c_i/c_0$, where i = 1,2,3. The constants are chosen to fit the behavior of single crystals of barium titanate ($BaTiO_3$) at room temperature, taking $c_0 = 1$ GPa, a value for the spontaneous polarization of p_0=0.26 C/m^2, the relative spontaneous strains ε_a = -0.44% along a-axis and ε_c = 0.65% along c-axis [15, 39]. The domain wall scaling parameter is set to $a_0 = 3.7 \times 10^{-9}\frac{\mathrm{Vm}^3}{\mathrm{C}}$ which leads to the value of 0.5 nanometer for the normalized unit length $\Delta x' = 1$. The normalized parameters are presented in Table 1. With the selected parameters, the normalized Landau-Devonshire energy is presented in Fig. 1 as a function of the normalized polarization p_1' and p_2', for a stress-free state ($\sigma_{ij} = 0$). Positive values of the energy are truncated to zero in

Table 1: Normalized parameters

c_1'	c_2'	c_3'	b_1'	b_2'	b_3'	α_1'	α_{11}'
185	111	74	1.4282	-0.185	0.8066	-0.0023	-0.0029
α_{12}'		α_{111}'	α_{112}'	α_{1111}'	α_{1112}'	α_{1122}'	ε_0'
-0.0011		0.003	-0.00068	0.001	0.0093	1.24	0.131

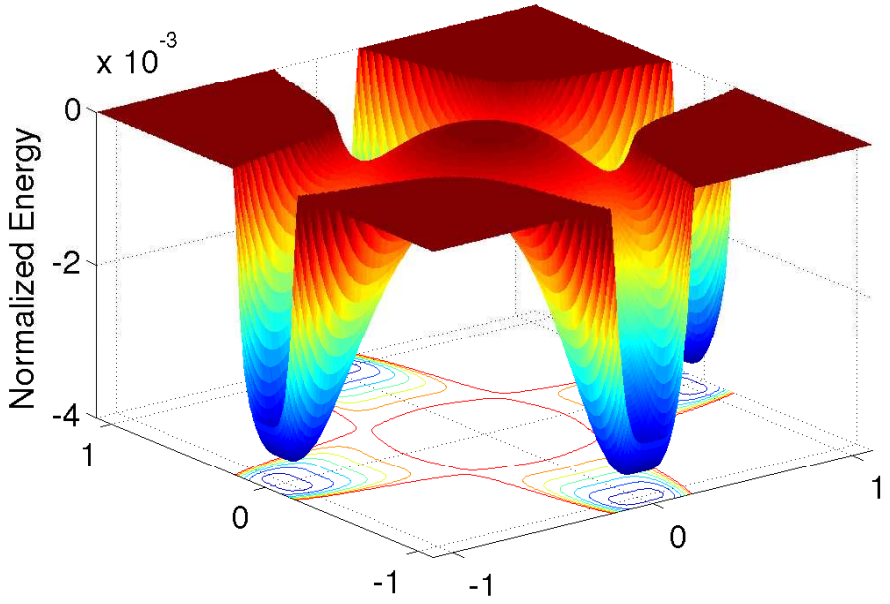

Figure 1: Normalized Landau-Devonshire energy density as a function of the normalized polarization components p'_1 and p'_2 in a stress-free state. Positive values are truncated to zero for clarity.

the plot, to highlight the energy landscape near the minima. The four minima in Fig. 1 correspond to the four variants of the tetragonal phase with normalized polarization $p' =$ (1,0),(0,1),(-1,0) and (0,-1).

Ignoring body loads and volume charges for simplicity, the total electro-mechanical enthalpy of a ferroelectric single crystal can then be written as

$$H[\boldsymbol{u}, \mathbf{p}, \phi] = \int_\Omega h(\boldsymbol{\varepsilon}(\boldsymbol{u}), \mathbf{p}, \nabla \mathbf{p}, \mathbf{E}(\phi)) \mathrm{d}\Omega - \int_{\Gamma_{N,\boldsymbol{u}}} \boldsymbol{t} \cdot \boldsymbol{u} \, \mathrm{d}S + \int_{\Gamma_{N,\phi}} \omega\phi \, \mathrm{d}S, \tag{6}$$

where $\boldsymbol{t}$ and ω are the tractions and surface charge density respectively, and $\Gamma_{N,\boldsymbol{u}}$ and $\Gamma_{N,\phi}$ are the parts of the boundary of the domain $\partial\Omega$ where mechanical and electrical Neumann boundary conditions are applied. By selecting the polarization as the primary order parameter [15], the time evolution of the system results from a gradient flow of the total electro-mechanical enthalpy with respect to the polarization, assuming that the displacement and the electric field adjust immediately to mechanical and electrostatic equilibrium (with infinite mobility), i.e.

$$\mu \int_\Omega \dot{p}_i \delta p_i \mathrm{d}\Omega = -\delta H[\boldsymbol{u}, \mathbf{p}, \phi; \delta \boldsymbol{p}], \quad 0 = \delta H[\boldsymbol{u}, \mathbf{p}, \phi; \delta \boldsymbol{u}], \quad 0 = -\delta H[\boldsymbol{u}, \mathbf{p}, \phi; \delta \phi], \tag{7}$$

for all admissible variations of the displacements, the polarization and the electric field, and where $1/\mu > 0$ is the mobility of the process. The form of the variations of the electro-mechanical enthalpy is given in Section 2.3, for the coupled model.

2.2. Phase-field model for brittle fracture

Following [27], we adopt a variational regularized view of Griffith's fracture theory. The total energy of a body made of brittle material and occupying a region Ω is written as:

$$E_\kappa[\boldsymbol{u}, v] = \int_\Omega (v^2 + \eta_\kappa) F(\boldsymbol{\varepsilon}(\boldsymbol{u}))\ \mathrm{d}\Omega + G_c \int_\Omega \left[\frac{(1-v)^2}{4\kappa} + \kappa |\nabla v|^2 \right]\ \mathrm{d}\Omega - \int_{\Gamma_{N,\boldsymbol{u}}} \boldsymbol{t} \cdot \boldsymbol{u}\ \mathrm{d}S, \quad (8)$$

where F is the elastic potential as a function of the strain $\boldsymbol{\varepsilon}$, and G_c is the critical energy release rate or the surface energy density in Griffith's theory [40]. The elastic potential F is the stored energy density as a result of deformation of an elastic body. For a linear elastic material, this potential is a quadratic function of the strain, i.e. $F(\boldsymbol{\varepsilon}(\boldsymbol{u})) = \frac{1}{2}\boldsymbol{\varepsilon}(\boldsymbol{u}) \colon \mathbf{C} \colon \boldsymbol{\varepsilon}(\boldsymbol{u})$, where $\mathbf{C}$ is the elastic stiffness tensor. The scalar field v provides a diffuse representation of the fracture zone, κ is a positive regularization constant to regulate the size of the fracture zone and η_κ is a small (relative to κ) residual stiffness to avoid the singularity of the first part of the energy in fully fractured regions of the domain. Natural boundary conditions are adopted for v. This functional is minimized in subsequent load increments, imposing additionally an irreversibility condition, namely that the field v (informally, a measure of the integrity of the material) can only decrease at any point in space during the incremental process. The minimizers of the total energy develop localized features, in particular localized regions with low or zero values of v, where the smeared crack is located.

It has been shown that, as long as η_κ converges to zero faster than κ, this regularized theory converges to the sharp theory of brittle fracture. Furthermore, it has been shown that the finite element discretization of this theory converges to Griffith's fracture theory when the mesh size and κ tend to zero in a concerted manner [29, 30], as described in Section 3.1.

The scalar field v is the phase-field parameter describing a smooth transition in space between unbroken ($v = 1$) and broken ($v = 0$) states of the material. By noting that v^2 multiplies the elastic potential F, it is clear that the value $v = 0$ effectively reduces the stiffness of the material to zero. When the regularization parameter κ tends to zero, this transition becomes sharper. It can be seen that in the limit of vanishingly small regularization parameter, the phase-field model exhibits traction-free solutions on the crack faces, as expected in the sharp crack model. For a finite but small value of the regularization parameter, as used in practical computations, the resulting solutions are very close to being traction-free in the smeared crack. For ferroelectric materials, similar conditions can also be considered for the electrical fields, as discussed in Section 2.3.

The first term in Eq. (8) can be interpreted as the bulk stored elastic energy, while the second takes the role of the surface energy. The crack propagation results from the competition between these two energy terms. When the elastic energy density F increases close to a critical value in a given region, it may become energetically favorable for the system to decrease the value of v towards zero in that region in order to release elastic energy. This comes at the expense of increasing the second term in the energy, since deviations from 1 are penalized. It is understandable then that the optimal solutions will release elastic energy by forming narrow regions of small values of v. However, since variations of v are also penalized in this second term, this model produces smeared cracks, whose width is governed by the

regularization parameter κ. The critical value for the elastic energy density is the energy level required to overcome the surface energy and to develop the fracture zone. By increasing the value of the critical energy release rate G_c of the material, the surface energy increases proportionally and it consequently requires a higher value of the elastic energy density to nucleate or propagate cracks. It can be checked mathematically that the integrand of the surface energy term converges to the surface area of the crack when κ tends to zero, as expected in the sharp interface model. For a finite but small value of κ, as used in practical computations, the second term will be a good approximation of the surface area of the smeared crack.

This total energy is nonlinear and non-convex as a function of two variables $\boldsymbol{u}$ and v, but for a linear elastic body, it is quadratic and convex in v and $\boldsymbol{u}$ separately. This observation has consequences in the efficient numerical implementation of this theory by means of an iterative algorithm. For a fixed v or $\boldsymbol{u}$, the minimizer of either $E_\kappa(\boldsymbol{u}, \bullet)$ or $E_\kappa(\bullet, v)$ exists, is unique, and can be efficiently computed solving a linear system of equations, with the appropriate boundary conditions [28, 29].

2.3. Brittle Fracture in Ferroelectric Ceramics

To study the quasi-static crack propagation in ferroelectric materials, we now form a total electro-mechanical enthalpy that includes the enthalpy of a possibly fractured ferroelectric material, together with the fracture surface energy. From a physical point of view, the presence of the crack affects only some of the contributions to the electro-mechanical enthalpy density h in Eq. (2). The specific coupling between the field v representing the crack and the other fields depends on the particular electrical and mechanical boundary conditions adopted for the crack. Note that in the phase-field model, these boundary conditions become part of the field equations since the crack faces are represented by an internal layer. By way of example, most of the crack models assume that the crack faces are mechanically traction-free, i.e. $\boldsymbol{\sigma} \cdot \boldsymbol{n} = 0$ on the crack faces, $\boldsymbol{n}$ being the unit outward normal. This condition is satisfied in the phase-field model for brittle fracture by multiplying the elastic energy density F by the jump set function $(v^2 + \eta_\kappa)$ (see Eq. (8)). Working by analogy, in the case of the proposed electro-mechanical model, we multiply the electro-elastic energy density W, which involves the elastic strains in all its terms, by the jump set function. We illustrate in Section 3 (see Fig. 8) that indeed this method produces numerical solutions satisfying the traction-free boundary conditions at the crack faces in an approximate but accurate way for a small yet finite value of the regularization parameter. For more technical details about this phase-field formulation of the boundary conditions on the crack faces, see [41].

When it comes to the electrical boundary conditions, there are two classical extreme assumptions, namely permeable and impermeable boundary conditions. The former were first proposed for electro-mechanical cracks [42] and assume that crack faces are closed and the electric field is not perturbed by the presence of the crack. Mathematically, these conditions lead to the continuity of the electric potential and the normal component of the electric displacement, i.e.

$$\phi^+ = \phi^- \qquad \text{and} \qquad \mathbf{D}^+ \cdot \boldsymbol{n}^+ = \mathbf{D}^- \cdot \boldsymbol{n}^-, \tag{9}$$

where the superscripts + and - denote the top and bottom crack faces. In order to encode these conditions in the phase-field model, the last two terms in the electro-mechanical enthalpy density h, which involve the electric field $\mathbf{E}$, should remain unmodified. In addition, free-polarization boundary conditions [43] are commonly assumed, implying that the gradients normal to the crack faces of the polarization components vanish at the crack faces, i.e.

$$\frac{d\mathrm{p}_i^+}{dn} = \frac{d\mathrm{p}_i^-}{dn} = 0, (i = 1, 2). \tag{10}$$

In the phase-field framework, we introduce this condition by multiplying the only term in h involving the gradient of polarization, i.e. the domain wall energy density U, by the jump set function $(v^2 + \eta_\kappa)$. The phase separation energy χ is not modified since it does not involve gradients of polarization. Besides, note that modifying also the phase separation energy would lead to an indeterminacy of the polarization inside the fracture zone. Figure 10, described later in detail, illustrates the smeared imposition of the free-polarization condition in the phase-field model.

In summary, for a traction-free, electrically permeable, and free-polarization crack, the electro-mechanical enthalpy density h follows

$$h(\boldsymbol{\varepsilon}, \mathbf{p}, \nabla\mathbf{p}, \mathbf{E}, v) = (v^2 + \eta_\kappa)\left[U(\nabla\mathbf{p}) + W(\mathbf{p}, \boldsymbol{\varepsilon})\right] + \chi(\mathbf{p}) - \frac{\varepsilon_0}{2}|\mathbf{E}|^2 - \mathbf{E}\cdot\mathbf{p} \tag{11}$$

where $(v^2 + \eta_\kappa)W + \chi$ is the modified Landau-Devonshire energy. Figure 2 shows cross sections of this energy at $p_2' = 0$ in the fractured ($v = 0$) and intact ($v = 1$) zones. The energy of the intact zone (solid line) is similar to Fig. 1 and the energy of a fractured region reduces to only the phase separation energy (dashed line). The minima of χ are located at $p_1' = \pm 0.86$ with an energy level of around half of that of the intact zone. The lower energy barrier enables to nucleate new domains in fractured regions. This makes it unnecessary to add noise or introduce nucleating defects to facilitate the nucleation of domains, as it is done in other works, e.g. [15].

In the other extreme case, impermeable boundary conditions were proposed to define an open and electrically defective crack by assuming zero permittivity for the crack gap [44]. In this model, the crack faces are treated as charge-free surfaces, i.e. the normal component of the electric displacement vanishes on both crack faces:

$$\mathbf{D}^+ \cdot \boldsymbol{n}^+ = \mathbf{D}^- \cdot \boldsymbol{n}^- = 0 \tag{12}$$

In contrast to the permeable crack, the impermeable crack does not sustain any electric displacement inside the fractured zone ($v = 0$) and thus the last two terms of the electro-mechanical enthalpy density h in (2) are multiplied by the jump set function $(v^2 + \eta_\kappa)$ accordingly. Numerical results in Section 3 (see Fig. 12) indicate that indeed the desired boundary condition on the crack faces is obtained with this method. See [41] for further details about this issue. Thus, for a traction-free, electrically impermeable, free-polarization crack, the electro-mechanical enthalpy density h takes the form

$$h(\boldsymbol{\varepsilon}, \mathbf{p}, \nabla\mathbf{p}, \mathbf{E}, v) = (v^2 + \eta_\kappa)\left[U(\nabla\mathbf{p}) + W(\mathbf{p}, \boldsymbol{\varepsilon}) - \frac{\varepsilon_0}{2}|\mathbf{E}|^2 - \mathbf{E}\cdot\mathbf{p}\right] + \chi(\mathbf{p}) \tag{13}$$

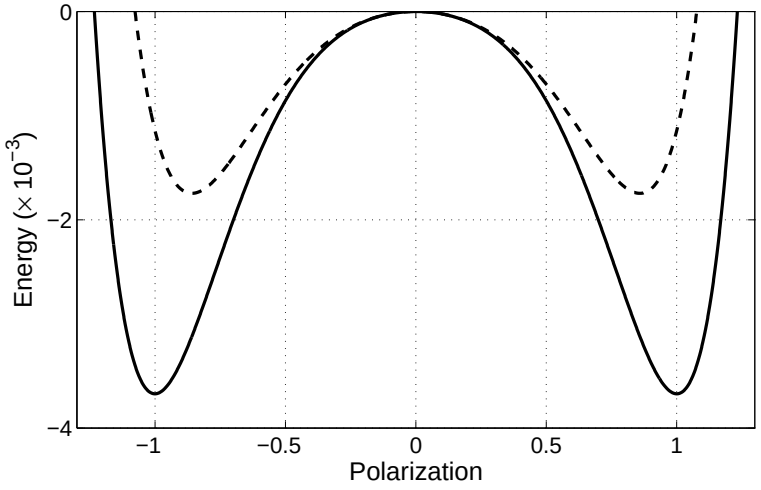

Figure 2: Normalized Landau-Devonshire energy density in the fracture (dashed line) and the intact (solid line) zones as a function of normalized polarization p_1' along $p_2' = 0$.

For both crack models, the total electro-mechanical enthalpy for a ferroelectric body occupying a region Ω is then

$$\begin{aligned} H[\boldsymbol{u}, v, \mathbf{p}, \phi] &= \int_\Omega h(\boldsymbol{\varepsilon}(\boldsymbol{u}), \mathbf{p}, \nabla \mathbf{p}, \mathbf{E}(\phi), v) \, \mathrm{d}\Omega \\ + G_c \int_\Omega \left[\frac{(1-v)^2}{4\kappa} + \kappa |\nabla v|^2 \right] \, \mathrm{d}\Omega &- \int_{\Gamma_{N,\boldsymbol{u}}} \boldsymbol{t} \cdot \boldsymbol{u} \, \mathrm{d}S + \int_{\Gamma_{N,\phi}} \omega\phi \, \mathrm{d}S. \end{aligned} \tag{14}$$

where the electro-mechanical enthalpy density h is given for permeable and impermeable cracks in (11) and (13), respectively.

The main objective of the coupled model is to capture interactions between the microstructure formation and evolution, and the crack propagation. The selection of the phase-field v as a secondary order parameter would lead to an immediate adjustment of v with infinite mobility. As a consequence, cracks would propagate much faster than the microstructure relaxation and the model would not be able to capture the microstructure evolution during the crack propagation. In the absence of detailed experimental or fundamental information on the relative kinetics of the microstructure evolution and the crack propagation, v is selected here, together with the polarization, as primary order parameters, and a finite mobility is introduced for the fracture process. Thus, the weak form of the gradient flow for the primary variables, together with the equations for mechanical and

electrostatic equilibria, follow from

$$\mu_p \int_\Omega \dot{p}_i \delta p_i \, \mathrm{d}\Omega = -\delta H[\boldsymbol{u}, v, \mathbf{p}, \phi; \delta \boldsymbol{p}] = -\int_\Omega \frac{\partial h}{\partial p_i} \delta p_i \, \mathrm{d}\Omega, \tag{15}$$

$$\begin{aligned} \mu_v \int_\Omega \dot{v} \delta v \, \mathrm{d}\Omega &= -\delta H[\boldsymbol{u}, v, \mathbf{p}, \phi; \delta v] \\ &= -\int_\Omega \frac{\partial h}{\partial v} \delta v \, \mathrm{d}\Omega - 2G_c \int_\Omega \left(\frac{v-1}{4\kappa} \delta v + \kappa v_{,i} \delta v_{,i} \right) \, \mathrm{d}\Omega, \end{aligned} \tag{16}$$

$$0 = \delta H[\boldsymbol{u}, v, \mathbf{p}, \phi; \delta \boldsymbol{u}] = \int_\Omega \frac{\partial h}{\partial \varepsilon_{ij}} \delta \varepsilon_{ij} \, \mathrm{d}\Omega - \int_{\Gamma_{N,\boldsymbol{u}}} t_i \delta u_i \, \mathrm{d}S, \tag{17}$$

$$0 = -\delta H[\boldsymbol{u}, v, \mathbf{p}, \phi; \delta \phi] = -\int_\Omega \frac{\partial h}{\partial E_i} \delta E_i \, \mathrm{d}\Omega - \int_{\Gamma_{N,\phi}} \omega \delta \phi \, \mathrm{d}S, \tag{18}$$

where $1/\mu_p > 0$ and $1/\mu_v > 0$ are the mobilities of the processes. The weak form of the evolution and equilibrium equations is discretized in space with standard finite elements. Equations (15) and (16) are discretized in time with a semi-implicit scheme from time t_m to $t_{m+1} = t_m + \Delta t_m$. A simple algorithm to solve the coupled system in a straightforward staggered approach is presented in Algorithm 1. This algorithm describes how to advance in one load step (or pseudo-time increment), and it is meant to achieve steady states for both ferroelectric domains and fracture processes in each load step. The functions $\boldsymbol{g}(t)$ and $f(t)$ encode the Dirichlet data for the mechanical displacement and electric potential as a function of the load step. After reaching a steady state for both the polarization and the phase-field v, the values for v^n, $\boldsymbol{u}^n$, $\mathbf{p}^n$ and ϕ^n are recorded and the algorithm proceeds to a new load at pseudo-time step t^{n+1}. Note that the values of v_{m-1} and ϕ_m are underlined in lines 8 and 9 of the algorithm to show that they are used only for the impermeable crack model.

Algorithm 1 for the coupled model

1: Let $m = 0$
2: Set $v_0 = 1$, $\mathbf{p}_0 = \mathbf{p}_{init}$, $\phi_0 = 0$ and $\boldsymbol{u}_0 = 0$ if $n = 0$
3: Set $v_0 = v^{n-1}$, $\boldsymbol{u}_0 = \boldsymbol{u}^{n-1}$, $\mathbf{p}_0 = \mathbf{p}^{n-1}$ and $\phi_0 = \phi^{n-1}$ if $n > 0$
4: **repeat**
5: $\quad m \longleftarrow m + 1$
6: $\quad$ Compute $\mathbf{p}_m$ in (15) using $\mathbf{p}_{m-1}$, $\boldsymbol{u}_{m-1}$, ϕ_{m-1} and v_{m-1}
7: $\quad$ Compute $\boldsymbol{u}_m$ in (17) using $\mathbf{p}_m$ and v_{m-1} under the constraint $\boldsymbol{u}_m = \boldsymbol{g}(t^n)$ on $\Gamma_{D,\boldsymbol{u}}$
8: $\quad$ Compute ϕ_m in (18) using $\mathbf{p}_m$ and $\underline{v_{m-1}}$ under the constraint $\phi_m = f(t^n)$ on $\Gamma_{D,\phi}$
9: $\quad$ Compute v_m in (16) using $\mathbf{p}_m$, $\boldsymbol{u}_m$, $\underline{\phi_m}$ and v_{m-1} under the constraint $v_m = 0$ for $v^{n-1} \leqslant \alpha$
10: **until** $\|\mathbf{p}_m - \mathbf{p}_{m-1}\|_\infty \leqslant \delta_{ferro}$ and $\|v_m - v_{m-1}\|_\infty \leqslant \delta_{vfield}$
11: Set $\boldsymbol{u}^n = \boldsymbol{u}_m$, $v^n = v_m$, $\mathbf{p}^n = \mathbf{p}_m$ and $\phi^n = \phi_m$

3. Numerical simulations

3.1. Computational domain and parameter setting

We consider a rectangular domain with the boundary conditions depicted in Fig. 3. The normalized dimensions of the domain are 200×200 and it is discretized with approximately 80,000 triangular finite elements of size $h \simeq 1$. A monotonically increasing mechanical load is applied by pulling the top and bottom sides of the model with a uniform vertical mechanical displacement such that $\boldsymbol{u}_{\pm} = (0, \pm t)$, where + and - indicate the top and bottom sides of the model respectively and t is the pseudo-time. The vertical mechanical displacement is also constrained at the top half and bottom half of the left side such that $u_{2\pm} = \pm t$. As this model does not have any pre-crack, this extra boundary condition forces the crack to initiate at the center-left of the model. For all the simulations, the initial polarization $\mathbf{p}_{init} = (1, 0)$ is assigned along the positive x_2 direction, see Fig. 3. Note that if the model is poled perpendicularly to the crack, then ferroelastic switching becomes unfavorable [2] and the interactions between the microstructure and the crack propagation become very weak. As for the electrical boundary conditions, the electric potential on the left and right sides of the domain is set to 0 and V respectively. Therefore, different electrical loadings can be applied in the horizontal direction by giving different values to V. Since the free-space dielectric constant is much smaller than that of the ferroelectric, it is assumed that the normal component of the electric displacement vanishes on other surfaces, i.e. $\mathbf{D} \cdot \mathbf{n} = 0$. All the boundaries are assumed to satisfy the free-polarization boundary condition, including the non-crack boundaries.

The intrinsic fracture toughness of $BaTiO_3$ is obtained from experimental results of an annealed sample as $K_c = 0.49$ MPa$\sqrt{m}$ [45]. The annealing procedure above the Curie temperature shifts the ferroelectric sample into the paraelectric state where domain switching cannot affect the measured fracture toughness. Considering Young's modulus and Poisson's ratio for $BaTiO_3$ as $E = 100$ GPa and $\nu = 0.37$ respectively (consistent with the elastic constants $c_i, i = 1, 2, 3$), the value of the critical energy release rate in plane strain is obtained as $G_c = \frac{(1-\nu^2)K_c^2}{E} = 2$ J/m^2. The value of normalized critical energy release rate is then calculated as $G_c' = G_c\sqrt{1/a_0 c_0}/p_0 = 4$.

The value of the fracture regularization parameter κ is chosen based on parametric studies of the discretized surface energy [29, 30]. It was shown that with linear triangular elements the surface energy is overestimated by a factor $1 + h/4\kappa$. For an accurate discretized surface energy, the element size h should be much smaller than the regularization parameter κ, i.e. $h/\kappa \ll 1$. In addition, the regularized formulation requires a sufficiently small value of κ relative to the other dimensions in the problem, for an accurate approximation of the sharp-interface model of brittle fracture. As a consequence, extremely fine meshes would be needed to fulfill strictly these conditions. The computational cost of such large meshes becomes more pronounced for the coupled model with six degrees of freedom per node in the case of plane polarization and strain. Numerical experiments indicate that setting $\kappa \sim h$ gives reasonable results, although the computed surface energy can be expected to be slightly overestimated [29, 30]. In our simulations, the regularization parameter is set to twice the

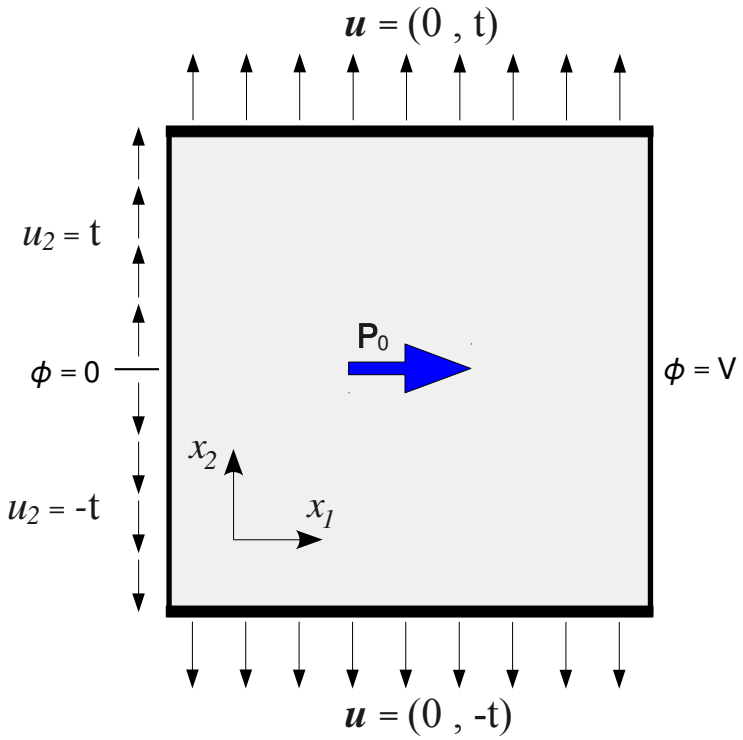

Figure 3: Computational model with boundary conditions; the initial polarization $\mathbf{p}_0$ is along the positive x_1 direction. The origin of the coordinate system is located in the left-bottom corner of the model. The non-dimensional size of the sample is 200×200.

element size as $\kappa = 2$, i.e. $h/\kappa = 0.5$.

The residual stiffness η_κ must be chosen as small as possible not to add large artificial stiffness and permittivity to the elements in the fracture zone. On the other hand, it must be large enough to guarantee non-singularity of the stiffness matrices used for the solution of finite element equations. These restrictions are usually satisfied by choosing the residual stiffness in the order of $\kappa \times 10^{-6}$ [28]. Here this value is set to $\eta_\kappa = 10^{-6}$ without any observed numerical instabilities in the simulations.

The normalized scaling parameter of the domain wall energy a_0' is used to adjust the domain wall width in the computational domain. This parameter has to be chosen such that the variation of the polarization can be resolved by the discretization while domain walls remain sufficiently sharp relative to other dimensions in the problem. These conditions are met in the simulations by setting $a_0' = 0.1$. The domain walls width is then spanned with 4-6 elements in the simulations, corresponding to 2-3 nanometers, in the order of experimentally measured values in tetragonal ferroelectric ceramics [46, 47].

The remaining constants are chosen as follows. The tolerances to achieve steady states for ferroelectric domains and fracture processes to $\delta_{ferro} = \delta_{vfield} = 10^{-3}$, the threshold to detect the irreversibly fractured regions to $\alpha = 2 \times 10^{-2}$, and the inverse mobilities to $\mu_p = 1$ and $\mu_v = 15$. One hundred load increments are performed in each simulation ($n = 100$)

with the pseudo-time interval of $\Delta t^n = 3 \times 10^{-2}$. Also the normalized time step $\Delta t'_m = 0.1$ leads to convergent and accurate solutions for the semi-implicit integration of gradient flow equations in (15) and (16). The simulations are carried out on parallel processors using the finite element library of the Kratos multi-physics package [48].

3.2. Mechanical loading

First, the sample is subjected to the mechanical loading alone – the electric potential on the left and right sides of the sample being fixed to zero ($V = 0$) – and both the permeable and impermeable crack models are considered.

3.2.1. Permeable crack

For the case of permeable crack, as the load increases, the field v starts to decrease around the center-left point of the sample until it reaches the threshold to be considered permanently fractured ($v < 0.02$) at load step $t = 0.9$ and the crack initiates. The contour of v in a small rectangle around this initiation point is presented in Fig. 4(a). Concurrently, the polarization vectors near the fracture initiation zone start to change their orientations towards the vertical direction as shown in Fig. 4(b). This 90^o ferroelastic domain switching is due to high tensile stresses around the fracture zone. By increasing the stresses during the following load steps, the crack propagates and the domain of vertical polarization grows gradually. Four snapshots of this evolution are shown in Fig. 5. In early stages, the switched regions form wing-shaped twins ahead of the crack tip, see Fig. 5(a), in qualitative agreement with the results of the small-scale switching model in [13]. These twins grow as the load increases until they reach the boundary of the sample at top and bottom sides. At this point, the domain switching propagates through the whole sample. Since the the top and bottom of the model are open-circuited, i.e. $\mathbf{D} \cdot \boldsymbol{n} = 0$, further growth of the domain is accommodated by the formation of multiple twins consistent with this boundary condition, see Fig. 5(b).

Note that here the boundary conditions help us form this special microstructure ahead of the crack path. These conditions may be interpreted physically as the effect of material defects or impurities, which lead to the formation of a multiple-domain structure ahead of the crack tip. For instance, the experimental results of [49] reported the formation of cross-needle-shaped micro-domains ahead of the crack tip. After the reported twinning event, the crack continues to propagate through the sample separating the twins. Figures 5(c) and 5(d) shows two snapshots in this regime.

To evaluate the effect of twinning on the crack propagation, the evolution of the normalized surface energy (the second integral in (14)) is presented in Fig. 6 as a function of the load step. Note that the surface energy is an indirect measure of the crack length. For comparison purposes, a graph is also produced for a single-phase material by running the simulation with a frozen polarization field set to $\mathbf{p}_{init}$. Since twinning does not happen in the single-phase model, its surface energy evolution can be viewed as a reference to be compared with the multi-phase model and assess the effect of twinning. The four snapshots presented in Figs. 5 are marked with the corresponding letters **a** - **d** in Fig. 6 for the permeable crack.

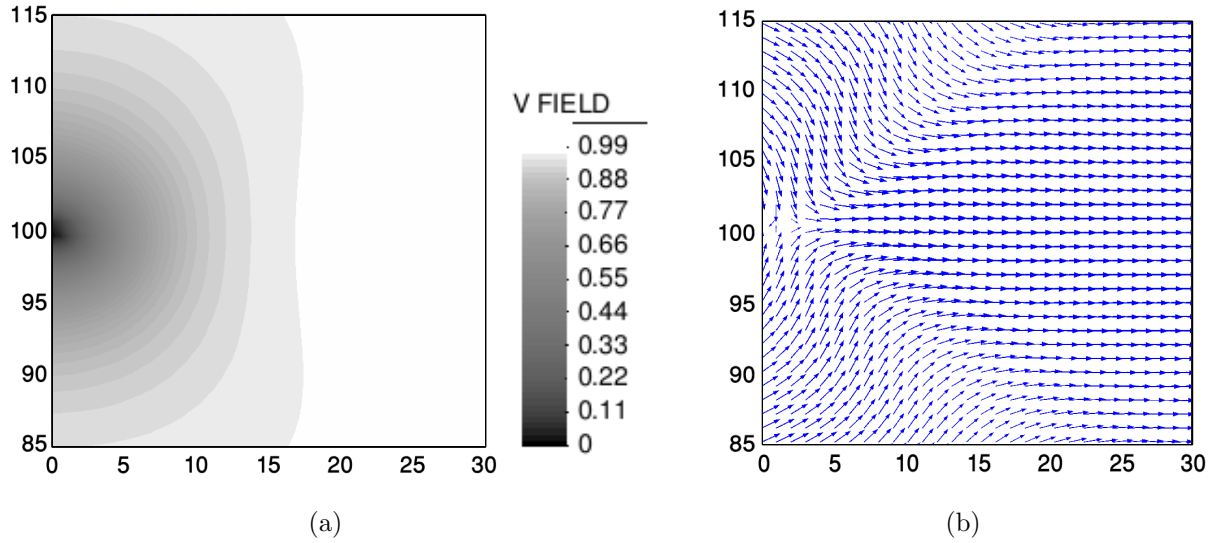

(a) (b)

Figure 4: Distribution of the primary order parameters v and $\mathbf{p}$ in a small neighborhood of the center-left point of the sample at load step $t = 0.9$ corresponding to crack initiation (a) contour of the field v (b) polarization vector field. Recall that the non-dimensional size of the sample is 200×200.

Both the single-phase and the multi-phase energy graphs start from zero (intact model), and are almost identical until the crack initiates for $t = 0.9$. After this point, the energies of the multi-phase models gradually depart from the single-phase graph and show a slower growth rate. This deviation is attributed to the retarding effect on the crack propagation of the 90^o ferroelastic domain switching in the vicinity of the crack tip illustrated in Fig. 4(b). Indeed, part of the high concentration of stored elastic energy near the crack tip can be released by aligning the longer axis of the crystal with the tensile stresses through switching rather than by propagating the crack. This effect becomes progressively more pronounced as the switched zone grows and wing-shaped twins appear ahead of the crack tip (load step **a**).

After reaching the energy level of about 200, the crack starts to propagate brutally, i.e. a small increase of the load leads to a big jump in the surface energy or the crack length. In the single-phase model, the brutal propagation is apparent around $t = 2.01$, and proceeds until the surface energy level reaches its maximum value of about 900 at load step $t = 2.16$. This maximum energy level indicates that the crack splits the model into two parts. On the other hand, the brutal crack propagation in the permeable multi-phase model starts at load step $t = 2.46$, when the crack leaves the first set of twins in its wake. Interestingly, the brutal propagation stops at load step $t = 2.49$ (step **b**) when multiple twins appear in front of the crack. This temporary crack arrest can be easily understood as follows. Since the crystal's unit cell is longer along the polarization direction, as encoded in the Landau-Devonshire model, compressive stresses in the x_2 direction are induced by the vertical twins, leading to a strong toughening effect, already pointed out in the literature [2]. Figure 7(b) highlights the σ_{22} stress components along the vertical twins (bold white) ahead of the crack at load

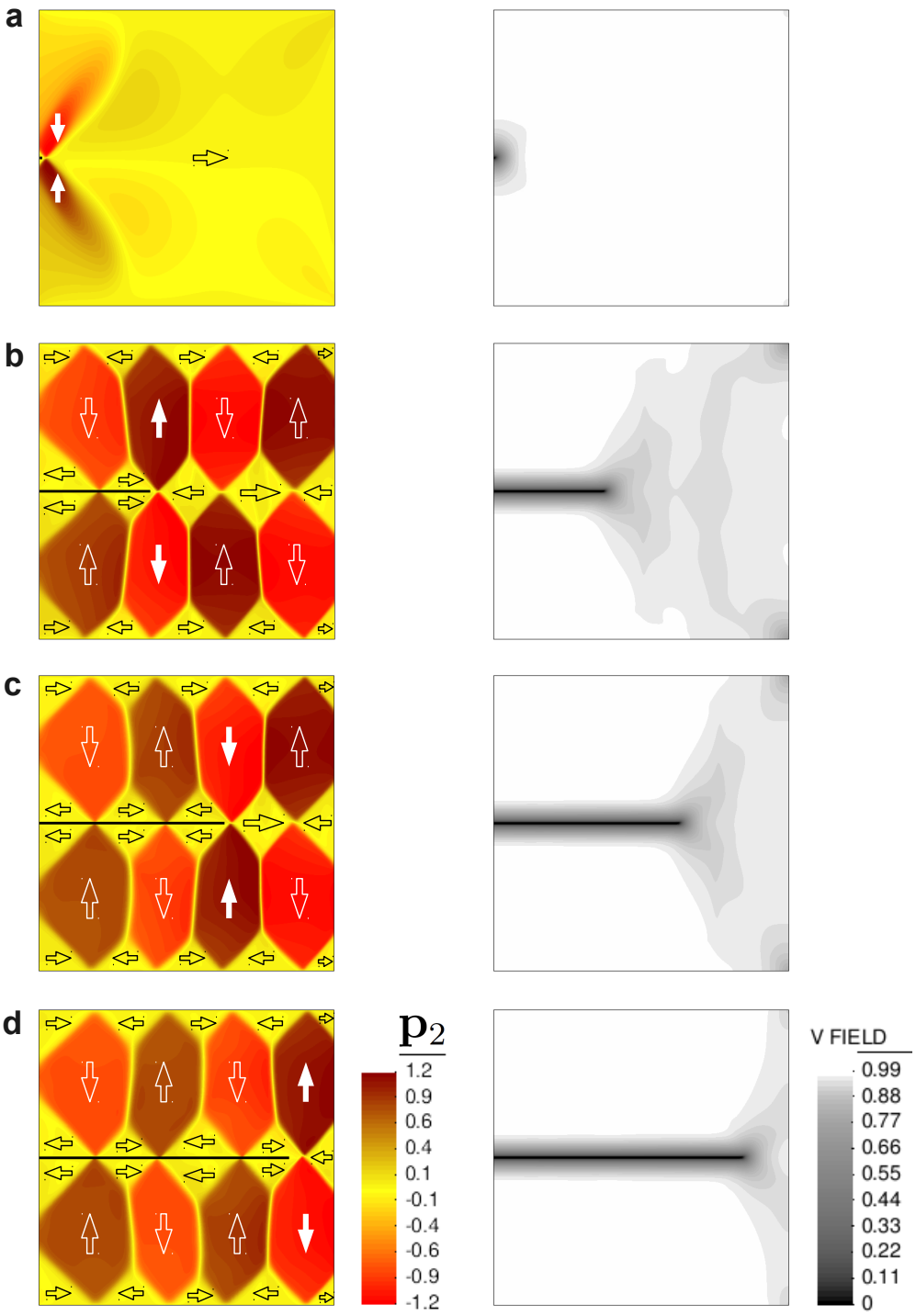

Figure 5: Four snapshots of the evolution of the microstructure and the permeable crack at load steps (a) $t = 1.05$, (b) $t = 2.49$, (c) $t = 2.58$ and (d) $t = 2.67$. The left column shows the vertical polarization field $\mathbf{p}_2$, which highlights the domain structure, and the right column shows the field v representing the fractured area. Domain orientations are indicated with large arrows, which are bold white for the twins ahead of the crack. The points where $v = 0$ are represented in black in the polarization maps to show the crack position.

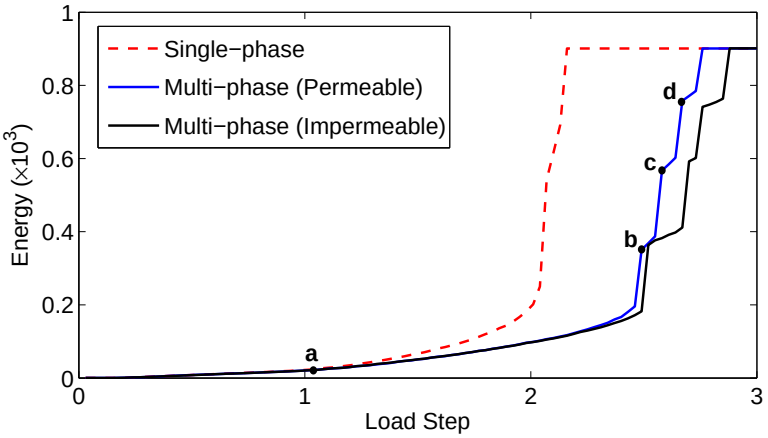

Figure 6: Evolution of the normalized surface energy as a function of the load step. The letters **a** – **d** correspond to the load steps shown in Fig. 5 for the permeable crack model.

step $t = 2.58$ (see Fig. 5(c)). These stresses are also plotted for the single-phase model with a crack of similar length for comparison. The reduction of the tensile stresses ahead of the crack tip caused by the twins is manifest in the figure, which hinders the crack propagation in the multi-phase model.

Due to this strong toughening effect, the crack propagation is significantly slower for the multi-phase model. A sequence of brutal crack propagation events, subsequent crack arrest, and slow crack propagation periods can be observed in Fig. 6. These stages reflect the following sequence of events. As the crack cuts a set of twins, it can propagate easily until it feels the compressive stresses of the next set of twins ahead of the tip, and it is arrested. Subsequently, it propagates slowly until the loading is high enough to overcome the compressive stresses due to the twins, and the process repeats itself. The snapshots in Fig. 5(c) and Fig. 5(d) correspond to slow propagation periods arrested by the twins ahead of the crack represented with bold white arrows. The corresponding points **c** and **d** in Fig. 6 indicate the starting points of the slow propagation periods. The sample finally splits into two parts in load step $t = 2.76$.

It is noteworthy that the experimental results in [49] show a similar slow-fast crack propagation behavior in a poled $BaTiO_3$ single crystal specimen under mechanical loading. This reference confirmed that the 90^o domain switching induced by the intense crack-tip stress field is the major mechanism behind the fracture toughening effect. This toughening mechanism is also reported in other experiments of crack propagation in $BaTiO_3$ [45, 50]. Our simulation capture many of the key features of these experimental observations. However, experimental observations by [49] reveal that the crack propagates along the cleavage plane [101] in $BaTiO_3$, following a zig-zag path that matches the domain pattern. This can be included in our model by considering an anisotropic critical energy release rate G_c, resulting in a lower surface energy or fracture toughness along the cleavage planes. This is the object of current work.

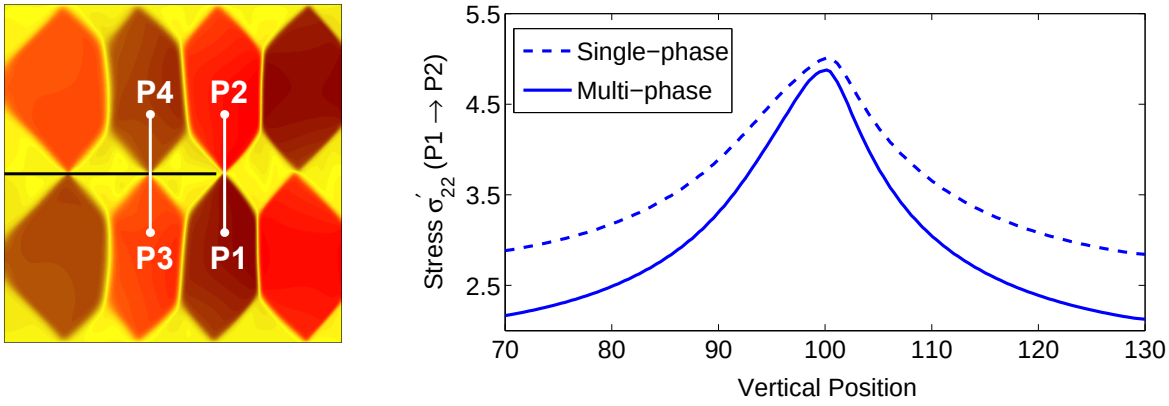

(a) (b)

Figure 7: (a) Position of the two cross sections: P1 → P2 along the twins in front of the crack tip, and P3 → P4 along one of the twins in the wake of the crack. The black line indicates the position of the crack. (b) Normalized stress σ'_{22} along the cross section P1 → P2 for the single- and multi-phase permeable crack models.

The stresses along a cross section of the sample behind the crack tip are presented in Fig. 8. The value of the field v is also plotted in this figure to indicate the cross section of the smeared crack. It is evident that all stress components vanish in the fractured zone ($v = 0$), since $\boldsymbol{\sigma} = \frac{\partial h}{\partial \boldsymbol{\varepsilon}} = (v^2 + \eta_\kappa)\frac{\partial W}{\partial \boldsymbol{\varepsilon}}$. Furthermore, the σ_{12} and σ_{22} stress components are close to zero at the edges of the smeared crack area, thus fulfilling the traction-free boundary conditions of the sharp crack model in an approximate but accurate way. In contrast, the σ_{11} stress component (not affected by the traction-free crack face condition) exhibits a non-zero value at the edges of the smeared crack.

3.2.2. Impermeable crack

Regarding the impermeable crack model, similar crack propagation and twinning events are observed in the simulation results. The corresponding energy graph in Fig. 6 also shows a slow-fast crack propagation behavior, but at a lower rate than that of the permeable crack model. This is apparent during slow crack propagation periods, and points out an additional effect of the twins on the impermeable crack besides the induced compressive stresses already mentioned for the permeable crack model. The origin of the slower crack propagation in the impermeable crack model can be understood from Fig. 9, depicting the magnitude of the electric field along the crack propagation direction near the permeable and impermeable crack tips. These graphs are obtained at the starting points of the third slow propagation period, i.e. load steps $t = 2.58$ (load step **c**) and $t = 2.7$ for the permeable and impermeable cracks, respectively. It is obvious that the impermeable crack conditions induce a significantly higher magnitude of the electric field, analogous to the stress concentration ahead of the crack tip. If the impermeable crack advances and cuts such a region of high electric field, it will release a certain amount of elastic energy, but at the expense of a high

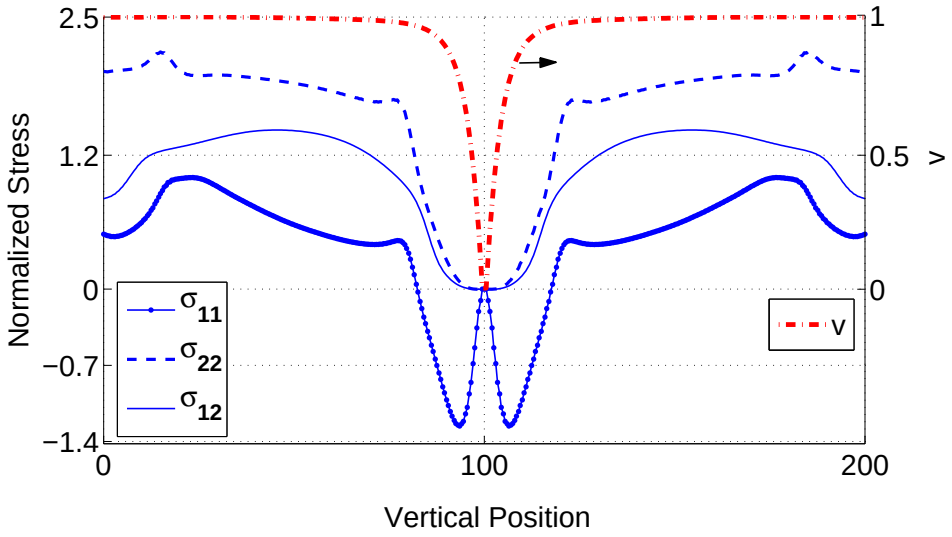

Figure 8: (Left) Normalized stresses along a cross section of the sample behind the crack tip for the multi-phase permeable crack model at load step **c** in Fig. 5, (Right) field v along the same section representing the smeared crack.

enthalpy increase due to the term $-\frac{\varepsilon_0}{2}|\mathbf{E}|^2$ in Eq. (13). Interestingly, this behavior has also been reported in experimental and analytical studies [51, 52, 53, 54].

Another difference between the results of the permeable and impermeable models is the distribution of the polarization along the twins in the wake of the crack. Figure 10 presents the vertical component of the polarization along one of these twins (see cross section P3 – P4 in Fig. 7(a)). Due to the free-polarization boundary conditions, the polarization approaches with zero slope the edges of the smeared crack for both crack models. In the case of the permeable crack, it follows a smooth transition across the smeared crack, and the jump becomes sharper as the value of κ decreases towards zero. In the case of the impermeable crack model, in addition to the free-polarization boundary conditions, the charge-free boundary condition (here $D_2 = 0$) should also be satisfied. Since for the sharp crack model $D_2 = p_2 + \varepsilon_0 E_2$, and E_2 is very small, this condition implies in fact that p_2 has to vanish at the edges of the smeared crack, which is apparent in Fig. 10.

The distribution of the electric displacement magnitude $|\mathbf{D}|$ is presented in Fig. 11(a) and 11(b) for the permeable and impermeable crack models, respectively, when approaching the vertical twins marked in Fig. 5(c). The position of the domain walls is highlighted by low values of the electric displacement, while the position of the crack is only apparent in Fig. 11(b). This figure shows that the impermeable crack is electrically defective, in agreement with the charge-free boundary condition. On the other hand, the permeable crack does not constitute an electrical barrier for the distribution of the electric displacement and the position of the crack is hardly detectable in Fig. 11(a). A smooth and small variation of the electric displacement around the permeable crack is attributed to stress-induced polarization fields near the crack.

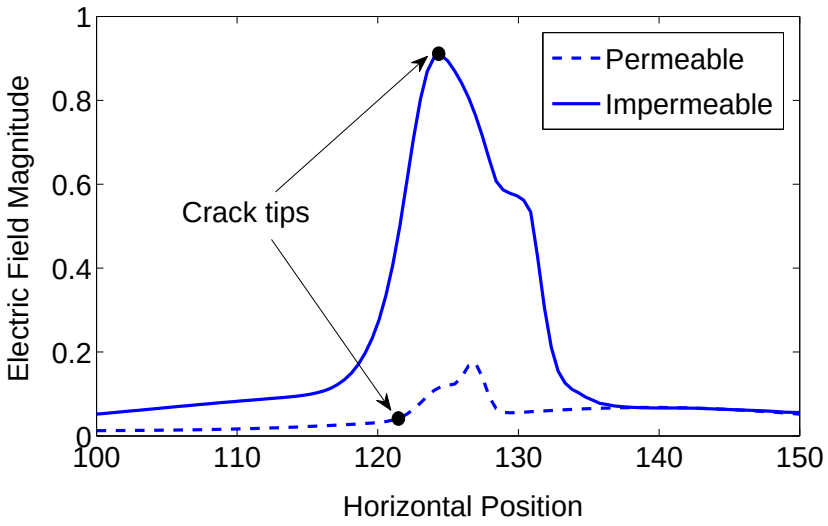

Figure 9: Electric field magnitude $|\mathbf{E}|$ along the crack propagation direction and near the crack tip.

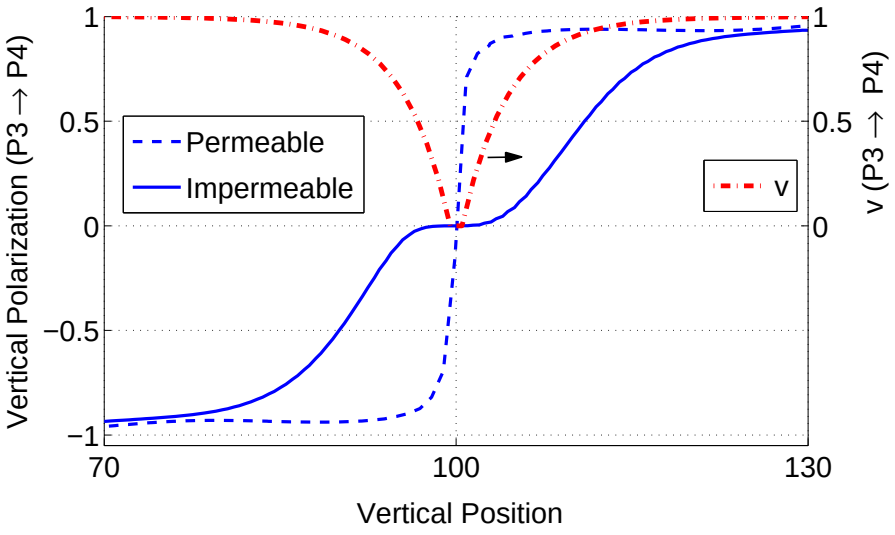

Figure 10: Vertical component of the polarization along the cross section P3 → P4 marked in Fig. 7(a) and field v representing the smeared crack.

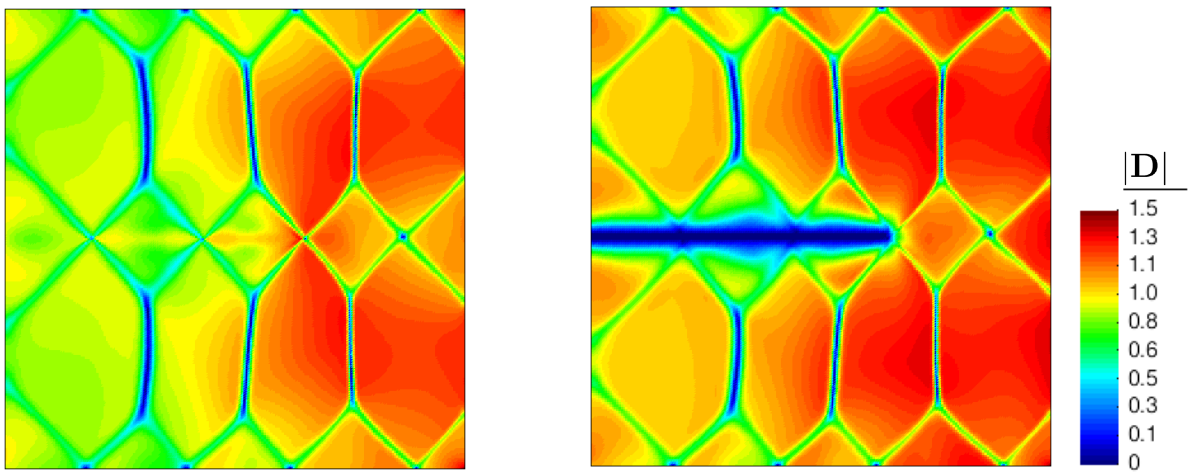

(a) (b)

Figure 11: Distribution of electric displacement magnitude $|\mathbf{D}|$ considering (a) permeable and (b) impermeable crack models.

Figure 12 highlights the vertical and horizontal components of the electric displacement and the field v along a cross section of the model behind the impermeable crack tip. It is apparent that both D_1 and D_2 vanish in the fractured zone ($v = 0$), as expected from $\mathbf{D} = -\partial h/\partial \mathbf{E} = (v^2 + \eta_\kappa)(\varepsilon_0 \mathbf{E} + \mathbf{p})$. The fact that the charge-free boundary condition of the sharp crack model is well approximated in the phase-field simulations is clear as D_2 vanishes at the edges of the smeared horizontal crack, while D_1 does not. Moreover, the boundary layers near the free and crack faces can be understood from the fact that inside the domain the electric displacement tries to align with the vertical polarization of the twins ($D_1 = 0$ and $D_2 \neq 0$), while at the boundaries and the crack it needs to remain horizontal ($D_1 \neq 0$ and $D_2 = 0$), thereby satisfying approximately yet accurately the charge-free boundary condition.

3.3. Electro-mechanical loading

Next, we perform simulations under combined electro-mechanical loading. A nominal electric field $E = -\frac{V}{L}$ is induced in the sample by setting the value of V, where L is the length of the sample. The behavior of the system is more complex in this case, since the electric field influences the size and position of the twins, as well as the polarization intensity. Our simulation results show that, by increasing the magnitude of the positive – along the poling direction – electric field, the coercive stress σ_c for 90^o ferroelastic domain switching increases and twinning becomes more difficult. A physical consequence is the gradual shrinking of the twins, de-twinning, ahead of the crack. An illustration of the twins forming under the positive electric field $E = 3 \times 10^{-3}$ is shown in Fig. 13(a) for the permeable crack model. It is apparent from this figure that the vertical twins (white arrows) decrease in size with respect to Fig. 5(d), while the horizontal domains (bold black arrows), which align as much as possible with the applied electric field, are significantly larger.

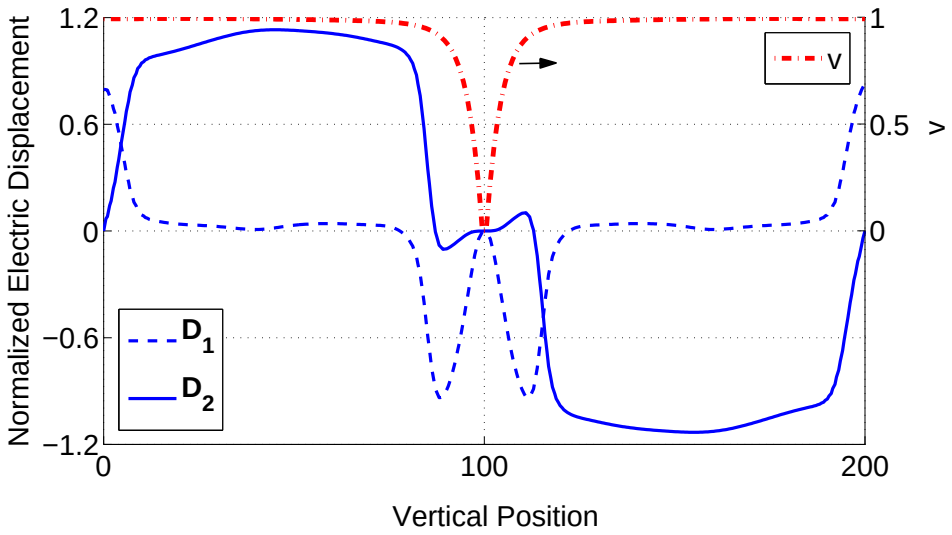

Figure 12: (Left) Normalized electric displacements along a cross section of the sample behind the crack tip for the multi-phase impermeable crack model, (right) field v along the same section representing the smeared crack.

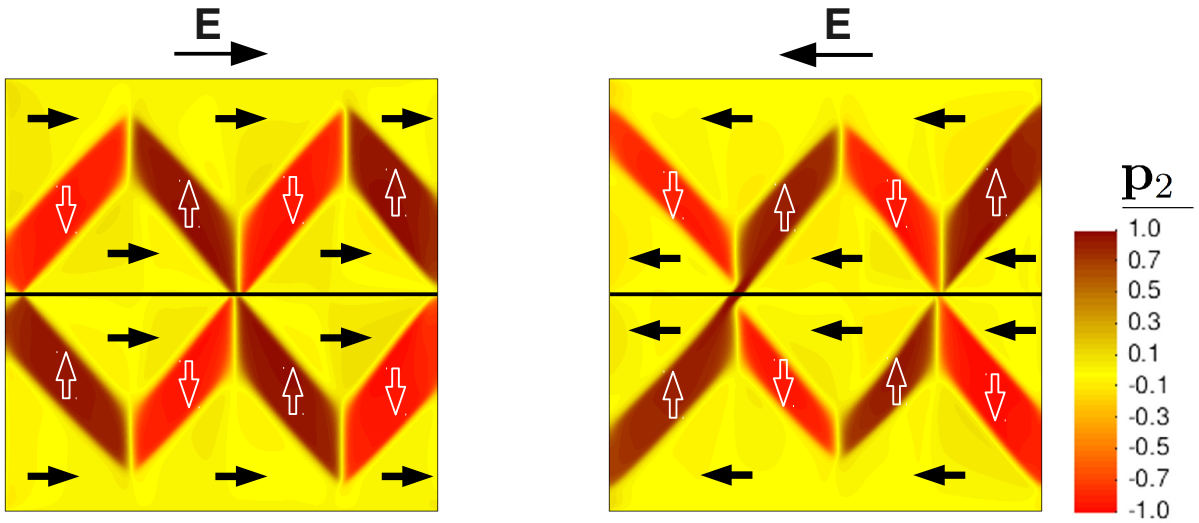

(a) (b)

Figure 13: Twinning in the permeable crack model under electro-mechanical loading (a) E = 3×10^{-3} (b) E =-4×10^{-3}. The black line shows the crack path and the bold black arrows indicate the domains aligned with the applied electric field.

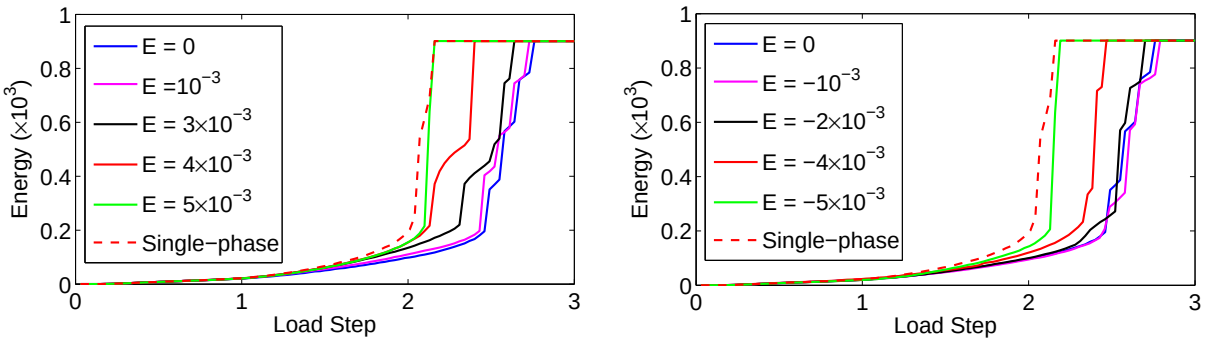

(a) (b)

Figure 14: Evolution of the normalized surface energy as a function of the load step for (a) positive – along the poling direction – and (b) negative – opposite to the poling direction – applied electric field in the permeable crack model.

To evaluate the effect of de-twinning on the crack propagation, the evolution of the normalized surface energy is presented in Fig. 14(a) for the permeable crack model considering different positive electric fields. As the electrical load increases, the crack splits the model under a lower load and the effective fracture toughness decreases approaching the single-phase model. The electric load also changes the position of the twins, and therefore biases the occurrence of the steps of slow-fast propagation. When the electric field increases to $E = 5 \times 10^{-3}$, only one set of small twins appears ahead of the crack, whose effect is the apparent slow propagation of the crack with respect to the single-phase model. The application of higher electric fields leads to the total de-twinning of the model, and the surface energy graphs are almost identical to that of the single-phase.

Turning to negative – opposite to the poling direction – electric fields, the energy graphs in Fig. 14(b) do not indicate a consistent toughening or weakening behavior for the low field magnitudes $E = -10^{-3}$ and $E = -2 \times 10^{-3}$. For an electric field of magnitude $E = -10^{-3}$, the 90^o ferroelastic domain switching becomes more favorable, and the twins become larger. The slight toughening enhancement with respect to the case $E = 0$ can be noticed in Fig. 14(b). As the magnitude of the negative electric field continues to increase, the polarization intensity decreases in the initial un-twinned sample, and after twinning occurs, the polarization of horizontally poled domains reverses. In this situation, a negative electric field of larger magnitude tends to de-twin the sample. Therefore, for negative applied fields, there is a competition between the toughening effect due to an enhanced 90^o ferroelastic domain switching and the weakening effect due to de-twinning. This is apparent in the energy graph of $E = -2 \times 10^{-3}$ as compared to $E = 0$. For stronger fields $E = -4 \times 10^{-3}$ and $E = -5 \times 10^{-3}$, the de-twinning effect is prominent and the model fails under a significantly lower load. A snapshot of the twins forming under a negative electric field $E = -4 \times 10^{-3}$ is shown in Fig. 13(b). Beyond $E = -5 \times 10^{-3}$, the whole model poles following the applied field and the fracture response is nearly identical to that of the single-phase model.

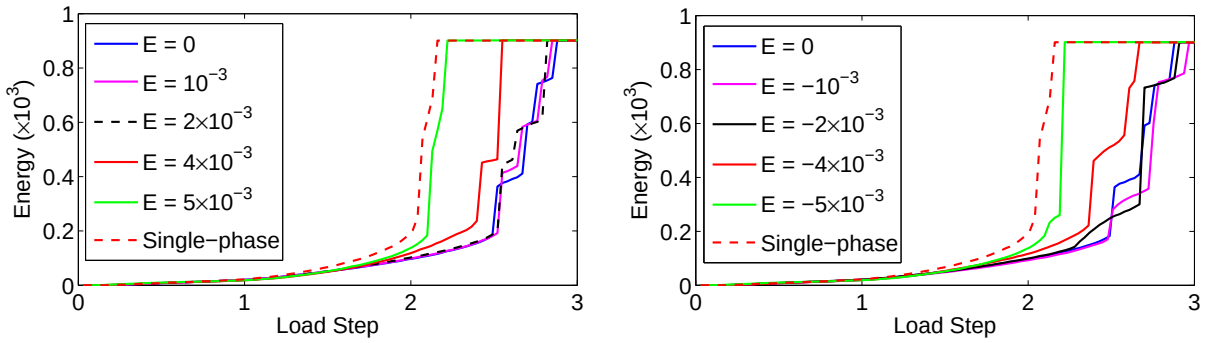

(a) (b)

Figure 15: Evolution of the normalized surface energy as a function of the load step for (a) positive – along the poling direction – and (b) negative – opposite to the poling direction – applied electric field in the impermeable crack model.

Regarding the impermeable crack, a similar de-twinning effect is observed in Fig. 15 for the high positive and negative electric fields. The energy graphs also show the same qualitative behavior as that of the permeable crack under low negative electric field magnitudes $E = -10^{-3}$ and $E = -2 \times 10^{-3}$. However, the impermeable crack does not show a consistent toughening or weakening behavior for the low positive electric fields $E = 10^{-3}$ and $E = 2 \times 10^{-3}$ in Fig. 15(a). Simulation results show that the applied electric fields are amplified by the twins in front of the crack tip and the retarding effect of the enthalpy terms associated with the electric field increases accordingly (see Section 3.2.2). This retarding effect diminishes as the positive electric field continues to increase and the model tends to be de-twinned. Therefore, for the impermeable crack under low positive fields, there is a competition between the toughening effect of the applied electric field and the weakening effect due to de-twinning.

4. Conclusions

We have presented a phase-field model for the coupled nucleation and evolution of cracks and domains in ferroelectric materials. The model naturally couples two energetic phase-field models for fracture and for the microstructure of such materials. We exercise the model in plane polarization and plane strain simulations of a sample under either mechanical or combined electro-mechanical loading conditions. The simulations reported here are, to the best of our knowledge, the first calculations for the fully coupled interaction between the crack propagation and the formation and evolution of microstructure in ferroelectric materials. We reproduce experimental observations, such as the slow-fast crack propagation due to the formation of twins in the vicinity of the crack tip and the retarding effect of the electric fields induced by these twins. Our simulations reveal a wealth of complex phenomena, for which competing effects make it difficult to interpret the experimental record. In particular, the simulations explain why for low applied electric fields below the coercive field, there is not a

clear shielding or weakening effect of the microstructure [52, 55]. Other experimental results also show that an enhanced crack propagation is obtained for parallel cracks under applied electric fields with the coercive magnitude [56]. This behavior agrees with the weakening effect of de-twinning for high magnitudes of applied electric field observed in the simulations.

The results reported here show the potential of our coupled phase-field model to elucidate the fracture behavior of ferroelectric ceramics, whose technological implications are very important. However, the work reported here also suggests that more work is needed to produce predictive simulations of such complex phenomena. In particular, as we have mentioned earlier, the anisotropy of the fracture behavior of ferroelectric single crystals seems to play an important role [49]. Also, it is widely accepted (and shown here as well) that the crack face electro-mechanical boundary conditions strongly affect the crack propagation in piezoelectric and ferroelectric ceramics, and thus more physically realistic crack conditions should be analyzed. Another important issue is the quantification and relative magnitude of the parameters μ_p and μ_v, which can have an important effect on the resulting response. All these topics are under investigation.

Acknowledgements

The authors gratefully acknowledge the support of the Ministerio de Ciencia e Innovación (DPI2007-61054).

References

[1] Zhang T, Gao C. Theor Appl Fracture Mech 2004;41:339.

[2] Schneider G. Annu Rev Mater Res 2007;37:491.

[3] Kuna M. Eng Fracture Mech 2010;77:309.

[4] Han X, Li X, Mao SX. Metall Mater Trans A 2002;33:2835.

[5] Rajapakse RKND, Zeng X. Acta Mater 2001;49:877.

[6] Beom H, Atlurib S. J Mech Phys Solids 2003;51:1107.

[7] Sheng J, Landis C. Int J Fracture 2007;143:161.

[8] Hackemann S, Pfeiffer W. J Eur Ceram Soc 2003;23:141.

[9] McMeeking R, Landis C. Int J Eng Sci 2002;40:1553.

[10] Wang J, Landis C. J Mech Mater and Struct 2006;1:1075.

[11] Hwang S, Lynch C, McMeeking R. Acta Mater 1995;43:2073.

[12] Zhu T, Yang W. Acta Mater 1997;45:4695.

[13] Yang W, Zhu T. J Mech Phys Solids 1998;46:291.

[14] Zhu T, Yang W. J Mech Phys Solids 1999;47:81.

[15] Zhang W, Bhattacharya K. Acta Mater 2005;53:185.

[16] Schrade D, Mueller R, Xu B, Gross D. Comput Methods Appl Mech Eng 2007;196:4365.

[17] Xu B, Schrade D, Mueller R, Gross D. Comput Mater Sci 2009;45:832.

[18] Su Y, Landis C. J Mech Phys Solids 2007;55:280.

[19] Dayal K, Bhattacharya K. Acta Mater 2007;55:1907.

[20] Desimone A. J Intell Mater Syst Struct 1994;5:787.

[21] Desimone A. Z Angew Math Mech 1996;76:397.

[22] Wang J, Zhang TY. Acta Mater 2007;55:2465.

[23] Song Y, Soh A, Ni Y. J Phys D: Appl Phys 2007;40:1175.

[24] Arias I, Serebrinsky S, Ortiz M. Acta Mater 2006;54:975.

[25] Gao H, Zhang T, Tong P. J Mech Phys Solids 1997;45:491.

[26] Francfort G, Marigo JJ. J Mech Phys Solids 1998;46:1319.

[27] Bourdin B, Francfort G, Marigo JJ. J Mech Phys Solids 2000;48:797.

[28] Bourdin B. Interfaces Free Bound 2007;9:411.

[29] Bourdin B, Francfort G, Marigo JJ. J Elast 2008;91:5.

[30] Amor H, Marigo JJ, Maurini C. J Mech Phys Solids 2009;57:1209.

[31] Xu X, Needleman A. J Mech Phys Solids 1994;42:1397.

[32] Camacho G, Ortiz M. Int J Num Methods Eng 1996;33:2899.

[33] Moes N, Dolbow J, Belytschko T. Int J Num Methods Eng 1999;46:131.

[34] Oliver J, Huespe A, Pulido M, Chaves E. Eng Fracture Mech 2002;69:113.

[35] JiangYu L. Mech Mater 2009;41:1125.

[36] Devonshire A. Philos Mag 1949;40:1040.

[37] Devonshire A. Philos Mag 1951;42:1065.

[38] Li YL, Cross LE, Chen LQ. J Appl Phys 2005;98:064101.

[39] Wang YL, Tagantsev AK, Damjanovic D, Setter N, Yarmarkin NVK, Sokolov AI, et al. J Appl Phys 2007;101:104115.

[40] Griffith A. Philos Trans Royal Soc London 1921;Series A-221:163.

[41] Abdollahi A, Arias I. In preparation 2011;.

[42] Parton V. Acta Astronautica 1976;3:671.

[43] Vendik OG, Zubko SP. J Appl Phys 2000;88:5343.

[44] Deeg W. PhD Thesis, Stanford University 1980;.

[45] Meschke F, Raddatz O, Kolleck A, Schneider G. J Am Ceram Soc 2000;83:353.

[46] Stemmer S, Streiffer S, Ernst F, Ruhle M. Phil Mag A 1995;71:713.

[47] Floquet N, Valot C, Mesnier M, Niepce J, Normand L, Thorel A, et al. J Phys III 1997;7:1105.

[48] Dadvand P, Rossi R, Onate E. Arch Comput Methods Eng 2010;17:253.

[49] Fang D, Jiang Y, Li S, Sun CT. Acta Mater 2007;55:5758.

[50] Meschke F, Kolleck A, Schneider GA. J Am Ceram Soc 1997;17:1143.

[51] Ricoeur A, Kuna M. J Eur Ceram Soc 2003;23:1313.

[52] Sun C, Park S. Ferroelectrics 2000;248:79.

[53] Li W, McMeeking R, Landis C. Eur J Mech A-Solids 2008;27:285.

[54] McMeeking R. Eng Fracture Mech 1999;64:217.

[55] Tobin AG, Pak YE. Proc SPIE, Smart Struct Mater 1993;1916:78.

[56] Schneider G, Heyer V. J Am Ceram Soc 1999;19:1299.